Dynamics of elastic biofilm threads

D.R. Espeso, A. Carpio

Centro Nacional de Biotecnologia, CSIC, Spain,
Departamento de Matematica Aplicada, Universidad Complutense de Madrid, Spain

Abstract

We investigate the formation of three dimensional patterns in bacterial biofilm filaments growing in flow circuits. Using a discrete rod formulation, we simulate behaviors observed in laboratory experiments. A continuous increase in length produces helical threads wrapped around the inner walls of cylindrical tubes. Coupling to a corner flow, straight filaments cross the mainstream to join opposite corners. The influence of parameters and boundary conditions is analyzed, revealing new features about the dynamics of these systems. Bacterial biofilms being ubiquitous in medical and industrial flow systems, our methods might help to understand their spread mechanisms.

Keywords: bacterial biofilms, elastic threads, helices, streamers, laminar flow, discrete rods

1. Introduction

The study of the bacterial behaviour in the environment must face the coupling between biological complexity and the different physical mechanisms involved at the considered scale [1]. This interaction affects these microorganisms at different levels and influences their behaviour drastically [2, 3].

Bacteria propagate through the environment by alternating both motile and sessile modes of life [2]. Although the planktonic state offers numerous advantages for a fast spreading in most habitats [4, 5], bacteria tend to form biofilms. Biofilms are bacterial aggregates embedded into a mixture of self-secreted chemicals with polymeric structure (also known as extracellular matrix, ECM) that attach firmly onto almost any surface [6, 7] and provide the mixture with a high resistance against environmental threats such as chemicals, predators or starvation [8, 9]. The composition and physical properties of this substance (i.e. viscosity, elastic constants, density, etc.) vary

greatly depending of the metabolic state of bacteria and the environmental conditions to which the biofilm is exposed [10], which leads to heterogeneous responses under different physical stimuli.

Submerged biofilms can spread swiftly using the environmental convection of the surrounding fluid as an effective transport mechanism, combined with detachment by shearing usually originated at the interface [7, 11, 8]. Fluid convection also interacts mechanically with biofilms shaping their biomass, which exhibits a viscoelastic nature [12]. Different experimental works document the formation of a rich variety of patterns when biofilms grow at different hydrodynamic regimes [13, 14], generally in straight rectangular channels. Recent studies emphasize the relevance of the geometry of the environment where biofilms spread, explaining the close relationship between biofilm nucleation, elastic behaviour of the biomass and observed patterns. Formation of bacterial streamers at corners [15] and of helicoidal threads in cylindrical tubes [16] under laminar flows are an example.

Bacterial spreading is a major topic in many fields of industry and science. Specially alarming is the colonization of human made environments such as medical and industrial habitats, where biofilms cause substantial economic losses [17, 18] and may threaten human life [8, 19, 20]. In silico studies can help to control biofilm expansion in these systems. However, developing effective computational models to simulate biofilm dynamics is a challenging task [21, 22, 23]. Successful simplified descriptions of biofilms can be found in the literature. Two phase flow models have successfully described pure growth due nutrient consumption [24] as well as complex osmosis processes by interaction with the substratum [25]. Flow induced motion has been studied as interaction between an elastic structure and a fluid [26, 27].

Although a full description of a biofilm should include complex features of bacteria such as chemotaxis, differentiation or gene expression [28, 29], which difficult their modeling and increase the computational effort, simple descriptions may be useful in specific contexts under specific circumstances. Some experiments [15, 16] suggest an approach in which biofims might behave as elastic bodies subject to a fluid - structure interaction, provided that certain conditions regarding the fluid dynamics and the biomass nature are fulfilled. These studies focus on the formation and evolution of biofilm threads, for which rod like descriptions balancing Euler-Bernouilli equations for an elastic beam with the viscous forces exerted by the fluid on the filament have been implemented in two dimensional settings [27].

We investigate the potential of using rods as mathematical modeling bod-

ies for describing filamentous biofilms. Rod descriptions are of interest because they allow for both mathematical analysis and low cost simulation, even in three dimensions. The modeling, analysis and simulation of elastic rods is an active discipline in different branches of mechanics [27, 30, 31, 32, 33], mathematics [34, 35, 36, 37, 38], and in computer animation [39]. Further applications in biology and medicine include medical equipment design and procedures [40, 41], DNA supercoiling analysis [42] and bacterial shape research [43].

Tradicionally, elastic rods have been studied by finite element [31, 42] or finite difference [36, 38, 43] discretizacions of the equations. Stable stationary configurations can be computed by energy minimization following gradient or geometric flows [35]. The introduction of specific representations of the rods, such as the Bishop frame, allows to simplify the analytical formulation and the numerical implementation of dynamic simulations [44, 45]. The rod is described by a curve (the centerline) plus an adapted material frame. Implicit treatments of the centerline built on reduced curvature coordinates have been implemented in computer graphics. However, explicit representations of the centerline in terms of edges and nodes or springs expedite the simulation of contacts and loops [46].

In this work, we focus on computing the elastic deformation of three dimensional biofilm threads due to perturbations such biological growth (considered as a continuous increase in length) and the presence of walls constraining displacement or geometry induced alterations in the flow. To this end, we will adapt discrete elastic rod models [46], incorporating wall constraints and coupling them to length variations and forces induced by the flow. We will apply the resulting equations to simulate helical biofilm growth in perturbed circular tubes and to reproduce the behavior of biofilm threads in three dimensional corner flows. Section 2 details the mathematical and physical framework. Section 3 discusses helix formation inside tubes. Section 4 considers flow induced thread bending. Finally, section 5 summarizes our conclusions.

2. Discrete elastic rod model

A thread is a geometric shape whose length is much larger than the rest of its dimensions. Any deformation in its cross section is expected to be small compared with the contributions along the total length. This fact motivates the description of a biofilm thread as a unidimensional curve γ (the

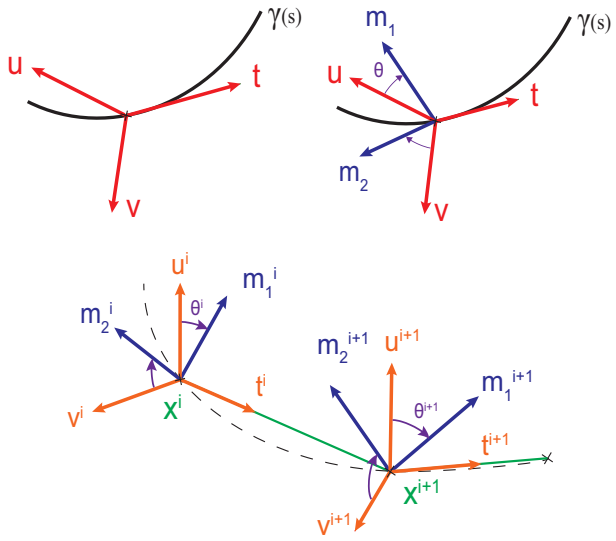

Figure 1: Squematic description of the reference systems for parallel transport in the (a) continuous and (b) discrete rod frameworks.

centerline) which characterizes its position. The mathematical framework to approximate an elastic rod by a unidimensional centerline was introduced in Ref. [45]. The configuration of the rod is represented by an adapted framed curve $\mathbf{\Gamma} = \{\gamma; \mathbf{t}, \mathbf{m}_1, \mathbf{m}_2\}$, see figure 1 (a). $\gamma(s)$ is the arc length parametrized centerline in $I\!R^3$. $\{\mathbf{t}(s), \mathbf{m}_1(s), \mathbf{m}_2(s)\}$ is an orthonormal material frame describing the local orientation. It is adapted to the curve in the sense that $\mathbf{t}(s) = \gamma'(s)$ is tangent to the curve. $\mathbf{t}' = \kappa$ is the curvature (normal) vector. The choice of the "rest orientation" for any point of the centerline is the Bishop frame $\mathbf{B}(s) = \{\mathbf{t}, \mathbf{u}, \mathbf{v}\}$: an adapted frame with no twist, i.e., $\mathbf{u}' \cdot \mathbf{v} = -\mathbf{v}' \cdot \mathbf{u}$. The assignment of the Bishop frame at the first endpoint of the curve ($s = 0$) completely determines it throughout the curve. With this description, the movement of the thread can be fully captured: stretching and bending are computed by deforming the centerline, whereas twisting is captured by the orientation of the material frame. Any twist undergone by the thread at any point will be computed as a rotation of $\mathbf{\Gamma}(s)$ an angle θ respect to $\mathbf{B}(s)$ around the plane delimited by $\{\mathbf{u}(s), \mathbf{v}(s)\}$, see figure 1(a). The relation between $\mathbf{m_1}, \mathbf{m_2}, \mathbf{u}, \mathbf{v}$ and θ is given by:

$$\mathbf{m_1} = \cos(\theta)\mathbf{u} + \sin(\theta)\mathbf{v}, \quad \mathbf{m_2} = -\sin(\theta)\mathbf{u} + \cos(\theta)\mathbf{v}. \tag{1}$$

A discrete version was introduced in Ref. [46] for computational purposes.

We recall it in the next subsection. Then, we indicate how to couple it to the force exerted by a fluid and how to take intro account the pertinent constraints.

2.1. Basic equations for a discrete Kirchoff rod

Following Ref. [46], an arbitrary centerline is discretized into a set of points $Q_n = \{\mathbf{x}_0, \mathbf{x}_1, ..., \mathbf{x}_{n+1}\}$ and straight segments joining them $\mathbf{e}^i = \{\mathbf{e}^0, \mathbf{e}^2, ..., \mathbf{e}^n\}$ where $\mathbf{e}^i = \mathbf{x}_{i+1} - \mathbf{x}_i$. A local orthonormal frame (the material frame) $M^i = \{\mathbf{t}^i, \mathbf{m}_1^i, \mathbf{m}_2^i\}$ describing the centerline orientation is assigned to each point, see figure 1(b). In an adapted frame, $\mathbf{t}^i = \frac{\mathbf{e}^i}{\|\mathbf{e}^i\|}$ is the unit tangent vector associated to each edge.

To define a Bishop frame we choose $\mathbf{u}^0 \perp \mathbf{t}^0$ and set $\mathbf{v}^0 = \mathbf{t}^0 \times \mathbf{u}^0$. The frames at the remaining edges are constructed by parallel transport [46]. We set

$$\mathbf{u}^i = P_i(\mathbf{u}^{i-1}), \quad \mathbf{v}^i = \mathbf{t}^i \times \mathbf{u}^i, \tag{2}$$

where P_i are rotation matrices about the curvature binormal defined by:

$$P_i(\mathbf{t}^{i-1}) = \mathbf{t}^i, \quad P_i(\mathbf{t}^{i-1} \times \mathbf{t}^i) = \mathbf{t}^{i-1} \times \mathbf{t}^i.$$

If $\mathbf{t}^{i-1} = \mathbf{t}^i$, P_i is the identity. The condition $\mathbf{u}^0 \perp \mathbf{t}^0$ must be maintained during the simulation. This is guaranteed when $\mathbf{t}^0$ is clamped. Otherwise, it can be reestablished by parallel transport in time (instead of space).

Known the angles θ^i defining the material frames by rotation of the Bishop frames, the material frame vectors at each edge are:

$$\mathbf{m_1^i} = \cos(\theta^i)\mathbf{u}^i + \sin(\theta^i)\mathbf{v}^i, \quad \mathbf{m_2^i} = -\sin(\theta^i)\mathbf{u}^i + \cos(\theta^i)\mathbf{v}^i. \tag{3}$$

When undeformed configuration of the rod is straight and its elastic response is isotropic, the elastic energy due to twisting and bending takes the form [46]:

$$E = \sum_{i=1}^{n} \beta \frac{(\theta^i - \theta^{i-1})^2}{\overline{\ell}^i} + \sum_{i=1}^{n} \frac{\alpha}{2\overline{\ell}^i} \sum_{j=i-1}^{i} \|\mathbf{w}_i^j - \overline{\mathbf{w}}_i^j\|^2, \tag{4}$$

where α and β are defined as $\alpha = E_Y I$ and $\beta = JG$, being E_Y the Young modulus of the thread, I the second moment of area, G the shear modulus of the thread and J the torsional rigidity constant. If we consider a thread

composed by an isotropic elastic material, the Young modulus and shear modulus are related by the Poisson coefficient ν as $G = \frac{E_Y}{2(1+\nu)}$. For a filled cylinder we have $J = I$, hence $\beta = \frac{E_Y}{2(1+\nu)} I$

$\overline{\ell}^i$ is the length of the segments $\overline{\mathbf{e}}^i = \overline{x}_{i+1} - \overline{x}_i$ in a reference undeformed configuration $\{\overline{\mathbf{x}}_0, \overline{\mathbf{x}}_1, ..., \overline{\mathbf{x}}_{n+1}\}$. The vectors $\mathbf{w}_i^j$, $\overline{\mathbf{w}}_i^j$, $j = i-1, i$, are material curvatures in the deformed and undeformed configurations, respectively:

$$\mathbf{w}_i^j = \left((\kappa\mathbf{b})_i \cdot \mathbf{m}_2^j, -(\kappa\mathbf{b})_i \cdot \mathbf{m}_1^j\right)^t, \quad (\kappa\mathbf{b})_i = \frac{2\mathbf{e}^{i-1} \times \mathbf{e}^i}{\|\overline{\mathbf{e}}^{i-1}\|\|\overline{\mathbf{e}}^i\| + \mathbf{e}^{i-1} \cdot \mathbf{e}^i}, \tag{5}$$

where $\kappa\mathbf{b}$ is the curvature binormal. The general form of the elastic energy for anisotropic rods that adopt a nonstraight undeformed shape is given in Ref. [46].

The material frame is updated in a quasistatic way. Imposing

$$\frac{\partial E}{\partial \theta^i} = 0, \tag{6}$$

for all segments i not fixed by a boundary condition, a system of equations determines the angle configuration that minimizes the energy of the rod. Clamped ends are accounted for assigning the material frame for $i = 0$ or $i = n$. No boundary condition corresponds to a stress free end.

The dynamics of the thread is computed by updating the displacement of the nodes according to Newton's second law:

$$\mathbf{M}\frac{d^2\mathbf{x}}{dt^2} = -\frac{dE}{d\mathbf{x}} + \mathbf{f}, \tag{7}$$

where $\mathbf{f}$ represents the external forces and $-\frac{dE}{d\mathbf{x}}$ the elastic forces. $\mathbf{M}$ is the mass matrix, which we take to be a multiple of the identity: $\mathbf{M} = m\mathbf{I}$.

To compute the evolution of a rod we proceed in the following steps [46]:

- Initialization:
  - Define the Bishop frame at edge 0: $(\mathbf{t^0}, \mathbf{u^0}, \mathbf{v^0})$.
  - Set the position of the undeformed centerline: $\overline{\mathbf{x}}_0, \overline{\mathbf{x}}_1, ..., \overline{\mathbf{x}}_{n+1}$.
  - Select the initial position and velocity of the centerline: $(\mathbf{x}_0, \dot{\mathbf{x}}_0)$, $(\mathbf{x}_1, \dot{\mathbf{x}}_1)$, ..., $(\mathbf{x}_{n+1}, \dot{\mathbf{x}}_{n+1})$.
  - Enforce the boundary conditions.

- Set the material curvatures using Eq. (5).
- Set the material frame by means of Eqs. (2), (3) and (6).

• Iteration:

- Compute the elastic forces $-\frac{dE}{d\mathbf{x}}$ acting on the centerline, and possible additional forces (see section 2.2).
- Integrate Newton equations for the centerline (7).
- Enforce inextensibility and other additional constraints (see section 2.3).
- Update the Bishop frame using Eq. (2).
- Update the quasistatic material frame by means of Eqs. (6) and (3).

2.2. Coupling to the flow

The force exerted by a fluid undergoing a given undisturbed flow on a long slender body is analyzed in Ref. [47]. The following asymptotic formula in terms of the ratio of the of the cross-sectional radius to the body length is given:

$$\frac{\mathbf{f}^t}{2\pi} = \mu_f \lambda \int_0^1 \Big(\Big[\frac{(\mathbf{u}-\mathbf{u}^*)^t}{\ln\,\kappa} + \frac{(\mathbf{u}-\mathbf{u}^*)^t \ln(2)}{(\ln\,\kappa)^2} \Big] \cdot [\mathbf{t}\,\mathbf{t}^t - 2\mathbf{I}] + \frac{\frac{1}{2}(\mathbf{u}-\mathbf{u}^*)^t}{(\ln\,\kappa)^2} \cdot [3\mathbf{t}\,\mathbf{t}^t - 2\mathbf{I}] \Big) ds, \tag{8}$$

where $\mathbf{f}$ is the force acting on a filamentous body of length λ, $\mathbf{u}$ and $\mathbf{u}^*$ are the velocities of the fluid and the thread, respectively, at the position $\gamma(s)$ and $\mathbf{I}$ is the identity matrix. We denote by μ_f the viscosity of the fluid, $\gamma(s)$ the position of the thread centerline, s the arclength of the thread ($0 < s < 1$), $\mathbf{t}(s) = \frac{d\gamma(s)}{ds}$ the tangent vector at the position $\gamma(s)$ and $\kappa = \frac{r}{L}$ the ratio between cross-sectional radius r to characteristic thread length L.

This relation allows us to directly calculate the external force $\mathbf{f}$ acting on each node of the thread by using the difference of velocities between the fluid and the thread, the tangent vector on each node and the aspect ratio of the thread.

2.3. Enforcing constraints

We apply a Verlet integrator to system (7) to estimate the displacements and velocities, and then enforce the inextensibility constrain for each segment by using a manifold projection method introduced in Ref. [48]. For each new time step, the Verlet scheme provides the prediction:

$$\tilde{\mathbf{v}}^{m+1} = \mathbf{v}^m - h\mathbf{M}^{-1}\mathbf{f}(\mathbf{x}^m), \quad \tilde{\mathbf{x}}^{m+1} = \mathbf{x}^m + h\tilde{\mathbf{v}}^{m+1}, \tag{9}$$

starting from previous values $\mathbf{x}^m, \mathbf{v}^m$, where $\mathbf{v}^m = \dot{\mathbf{x}}^m$ and h is the time step. The projection method works as follows. We set $\mathbf{y}_0 = \tilde{\mathbf{x}}^{m+1}$. At each step j, we compute the next value $\mathbf{y}_{j+1} = \mathbf{y}_j + \delta\mathbf{y}_{j+1}$, where

$$\delta\mathbf{y}_{j+1} = -h^2\mathbf{M}^{-1}\nabla\mathbf{C}(\mathbf{y}_j)^t\,\delta\ell_{j+1}, \tag{10}$$

and $\mathbf{C}(\mathbf{y})$ defines the system of constraints. The vector $\delta\ell_{j+1}$ solves the linear system

$$h^2\nabla\mathbf{C}(\mathbf{y}_j)\mathbf{M}^{-1}\nabla\mathbf{C}(\mathbf{y}_j)^t\,\delta\ell_{j+1} = \mathbf{C}(\mathbf{y}_j). \tag{11}$$

The iteration stops if $\|\mathbf{C}(\mathbf{y}_{j+1})\| \leq \varepsilon$ for the desired tolerance $\varepsilon > 0$. The constraint enforcing velocity and position are then

$$\mathbf{v}^{m+1} = \frac{1}{h}(\mathbf{y}_{j+1} - \tilde{\mathbf{x}}^{m+1}), \quad \mathbf{x}^{m+1} = \mathbf{x}^m + h\mathbf{v}^{m+1}. \tag{12}$$

If inextensibility is the only constraint, $\mathbf{C}$ is defined by the system of equations $\|\mathbf{e}^i\|^2/\|\overline{\mathbf{e}}^i\| - \|\overline{\mathbf{e}}^i\| = 0$, for each edge i.

Biofilm filaments live inside tubes of a certain shape. A simple way to incorporate this restriction is a penalty method. The idea is to add in equations (7) a large force supported on the tube walls that points inside the tube and acts on any node hitting the wall, sending it back inside. Alternatively, we might set the position equal to the effective maximum radius and reset the velocity equal to zero.

2.4. Increasing length

Increase in length of a filament can be described in several ways. In our physical setting, more biomass may accrues to the filament following a definite direction. This process can be represented adding nodes at that edge and redefining the reference configuration each time a node is added. Filament length can also increase due to biomass production all through the

thread. To reproduce this process, we enlarge the length between segments in a controlled way, redefining the reference lengths at the same time.

In practice, we alternate steps in which we solve the equations for the evolution of the discrete rod in which we increase the length of the edges or the number of nodes, and reset the reference configuration before computing again the evolution of the enlarged filament.

2.5. Nondimensional equations

We nondimesionalize the equations (4),(7),(8) for numerical purposes. The change of variables $x = \lambda x'$, $t = Tt'$, $\mathbf{u} = U_0\mathbf{u}'$, $E = \frac{\alpha}{\lambda}E'$, $\mathbf{f} = \mu_f \lambda U_0 \mathbf{f}'$ yields:

$$\frac{d^2\mathbf{x}'}{dt'^2} = -\frac{T^2}{m\lambda^2}\frac{dE}{d\mathbf{x}'} + \frac{T^2}{m\lambda}\mathbf{f} = -\frac{\alpha T^2}{m\lambda^3}\frac{dE'}{d\mathbf{x}'} + \frac{\mu_f U_0 T^2}{m}\mathbf{f}'. \tag{13}$$

In view of the definition (4) of the energy E, this change introduces the controlling parameters $\alpha' = \frac{\alpha T^2}{m\lambda^3}$, $\beta' = \frac{\beta T^2}{m\lambda^3}$ and $\delta' = \frac{\mu_f U_0 T^2}{m}$, U_0 being a characteristic velocity. Determining ranges of values of α', β' that lead to different types of filamentary structures we would obtain ranges for α, β whenever the density ρ and radius r of the filaments are experimentally quantified. Working with one dimensional filaments, we neglect the cross-sections. A three-dimensional cylindrical thread of density ρ, radius r, and length $L >> r$ is approximated in this setting by a discrete rod with N nodes and $N-1$ edges, with mass $m = \rho\pi r^2 L/(N-1)$. From identities (4) and (13), the characteristic time associated to the elastic deformation of the thread can be estimated as $T_{elast} = \sqrt{\frac{m\lambda^3}{E_Y I}}$. If this value is chosen as characteristic time in our system and we use formula (8) we arrive at:

$$\frac{d^2\mathbf{x}'}{dt'^2} = -\frac{dE'}{d\mathbf{x}'} + \eta\mathbf{f}', \tag{14}$$

where $\eta = \frac{\mu_f U_0 \lambda}{\frac{E_Y I}{\lambda^2}}$ is the ratio of viscous forces to elastic forces (see [27]).

All the simulation parameters referred in the next sections are given in dimensionless units.

3. Helicoidal biofilms in tubes

Our first case study is the formation of helicoidal patterns in tubes of circular section, see figure 2. These structures have been experimentally

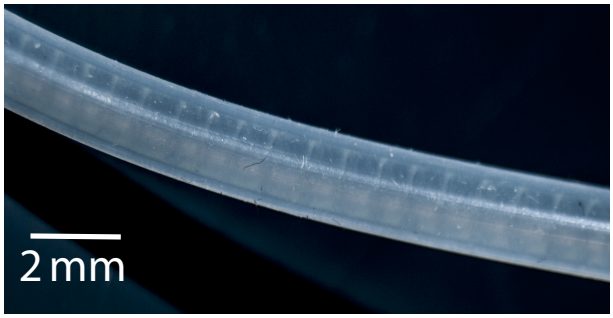

Figure 2: Biofilm helices formed by the strain *P. putida mt-2* inside a silicone tube. The image was treated to enhance contrast and shape.

observed in Ref. [16]. They seem to develop by a sequential process of biofilm accumulation, which evolves into a current of biomass slowly flowing downstream. This filamentous structure is deformed and reallocated through the development of a helical elastic instability. The whole process is driven by the net increase in length of the thread whose origin lies in both the bacterial metabolic activity and possible swelling phenomena.

Helical shapes are minimizers of elastic rod energies [49], frequently observed when perturbed straight filaments are constrained to remain inside a tube [32]. A twisted end is often the cause of helical instabilities [32, 46]. Here, the difference between the thread and tube lengths seems to furnish additional driving mechanisms.

3.1. Helix formation and wrapping around tubes

This scenario is simulated starting from a perturbed inextensible straight filament of length L taking as characteristic time $T = \sqrt{\alpha'} T_{elast}$ and as characteristic length $\lambda = 1\,mm$. Most of our simulations disturb the initial thread by randomly varying the node position. The thread is placed inside a cylindrical tube of diameter d_{tube} and length $L_{tube} < L$, see figure 3(a). To achieve helical structures as those reported in experiments, the excess length $L - L_{tube}$ must be large enough to allow for a sustained expansion of the helix until its radius equals the radius of the tube r_{tube}. If this requirement is not fullfilled, helical instabilities with smaller radius will be observed, unless the perturbation vanishes. The length ℓ, radius r and pitch h of a helix are related by $\ell = \sqrt{h^2 + 4\pi^2 r^2}$. Thus any thread with length L inside a tube of length L_{tube} and radius r_{tube} can develop a helical trajectory with k steps of pitch L_{tube}/k if $L^2 \geq L_{tube}^2 + 4\pi^2 r_{tube}^2 k^2$, that is, $k^2 \sim \frac{L^2 - L_{tube}^2}{4\pi^2 r_{tube}^2}$. These

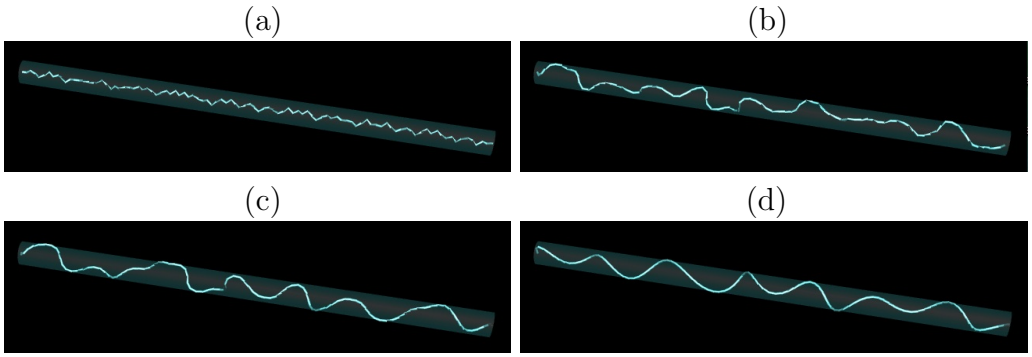

Figure 3: (a) Geometry and initial conditions: a randomly perturbed straight thread of fixed length L centered inside a tube of diameter d_{tube} and length $L_{tube} < L$. (b), (c) and (d) Evolution of the elastic filament at iterations 100, 250 and 1000 respectively. The filament expands and twists to reallocate its structure until it reaches the inner wall of the tube, finally adopting a helicoidal shape with a specific number of loops, selected by the thread length and the tube radius. Parameter values: $\alpha' = 4.345$, $\beta' = 5.789$, $\delta' = 0$, $nodes = 100$, $L = 53.67$ spatial units, $L_{tube} = 40$ spatial units, $d_{tube} = 2$ spatial units, $t_{max} = 1000$ iterations, $\theta_0 = 14\pi$, time step $\Delta\tau = 0.01$ time units.

relations define the equilibrium helical shapes that long enough threads tend to reach. The choice of elastic parameters and the imposed twist, may stop this evolution in a different stage, with smaller pitch and radius, or uneven steps. Also, for fixed elastic parameters and twist, too long initial threads might develop knots or vary in a disordered way.

Figure 3 and Supplementary Movie 1 show an example of the evolution described above. A perturbed thread of length 53.6 spatial units contained in a shorter tube of length 40 spatial units and located at the center of its radial section, evolves into a helix that wraps around the inner wall of the tube. The edges are clamped and a uniform twist of value $\theta_0 = 14\pi$ between both sides is imposed. The initial thread in figure 3(a) bends to accommodate the excess of length, generating a train of loops. The small loops in figure 3(b) compete between them to gain length at expense of the others, see figure 3(c). They expand radially until the helicoidal pattern is constrained by the wall and begins to wrap around it, as shown in figure 3(d). The thread adopts a helicoidal shape with a pitch step that minimizes the elastic energy stored in its structure. The thread can be initially locat ed either at the bottom of the tube or centered inside it. A similar evolution is observed, though, in the first case, helix formation is delayed.

The experimental study of helical biofilm evolution [16] suggests that

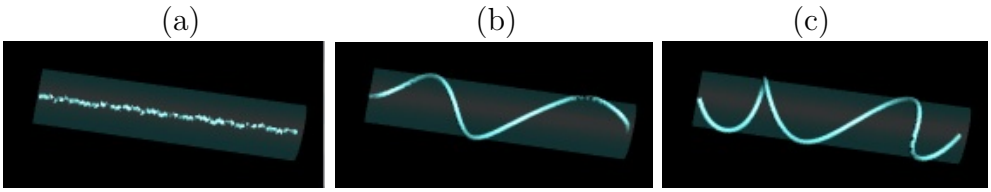

Figure 4: Evolution of a helix under a sustained length increase. Biomass production at a fixed rate fosters the radial expansion of the thread, increasing its length from an initial value of (a) 12.466 to (b) 13.260 and (c) 16.082 spatial units. Parameter values: $\alpha' = 4.345$, $\beta' = 5.789$, $\delta' = 0$, $nodes = 100$, $L_{tube} = 9.29$ spatial units, $d_{tube} = 2$ spatial units, $t_{max} = 6000$ iterations, $\theta_0 = 14\pi$, $\Delta\tau = 0.01$ time units. Length increase rate per edge $= 10^{-5}$ spatial units. Length increase rate for the thread$= 9.9 \times 10^{-4}$ spatial units/iteration.

these structures increase their length by the effect of bacterial activity that generates biomass over time. Eventually, other phenomena like swelling or stretching of that biomass may occur. Thus we envisaged a mechanism to increase the thread length during its deformation. After fixed time intervals, we enlarged the size of the thread by separating uniformly each node at a constant rate. Figure 4 shows a thread of initial length $L = 12.466$ spatial units being gradually enlarged until a final length of 16.082 spatial units is reached (a length increment of 29.01%). Length increase allows the thread to curl and reach the walls of the tubes, influencing its geometry, which finally adopts a helicoidal structure after 6000 iterations.

Biomass production allows filaments to grow and wrap around the inner walls of the tube keeping a small pitch despite the fact their initial length may not be enough to trigger helix formation. Figure 5 illustrates this process, showing a reorganization of the nodes to perform additional twists. The final result is a progressive decrease of the helix pitch and an increment in the number of observed helical steps (frequency).

In all cases, a balanced combination of elastic parameters is required to develop a well defined helicoidal geometry. The bending modulus α regulates the bending degree. Large enough values are required to unfold the structure into a helicoidal shape. As α grows, the number of loops decreases while their amplitude grows. Increasing values of α are needed to sustain a helicoidal geometry as its radius expands. Nevertheless, too large values of α result in numerical instability due to the inability to fulfill the inextensibility condition while being constrained inside the tube. The torsion modulus β controls the ability of the thread to twist. High enough values provide freedom to

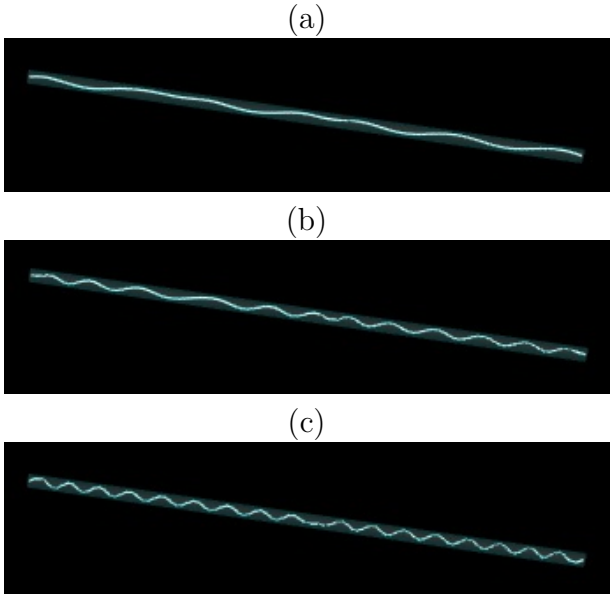

Figure 5: The helix step shrinks when the length of the thread increases due to biomass production. At iterations (a) 250, (b) 1500 and (c) 4200 the number of helical turns are 7, 12 and 17 respectively. Parameter values: $\alpha' = 10$, $\beta' = 0.5$, $\delta' = 0$, $nodes = 100$, $L = 20.001$ spatial units, $L_{tube} = 20$ spatial units, $d_{tube} = 0.2$ spatial units, $t_{max} = 4200$ iterations, $\theta_0 = 2\pi$, $\Delta\tau = 0.01$ time units. Length increase rate per edge $= 10^{-5}$ spatial units. Length increase rate for the thread$= 9.9 \times 10^{-4}$ spatial units/iteration.

move the nodes out of bending planes and relax the structure. However, too large values will delay the time needed to evolve into a helix or completely hinder the process by preventing proper unfolding. Too low values lead to oscillations in the node positions, thus delaying also the relaxation time. Increasing the twist between the thread edges may stabilize the evolution of long filaments.

The spatial discretization of the thread, defined by the number of nodes used to represent it, also affects the evolution. Few nodes will prevent smooth helix development. An excessive number of nodes induces numerical instability unless the time step is drastically reduced, exceedingly raising the cost. Furthermore, an increasing number of nodes leads to a reduction in the the length of the edges, which eventually will prompt numerical instability if the tolerance for the edge length at the fast manifold projection step is reduced. An increased computational effort is thus needed to preserve the inextensibility constrain.

Achieving a successful helical shape depends also on the radius/length ratio of the tube to fill. Our simulations resulted into helical structures for values of the radius/length ratio around 1/100 for a broad range of elastic parameters and $L - L_{tube}$ differences. For larger ratios, such as 1/10, these parameters become more difficult to adjust, and biomass production has to be included if ratios of 1/3-1/5 are desired. Figure 5 shows the evolution of an initial thread which grows in length at constant rate (9.9×10^{-4} spatial units/iteration) during 4200 iterations to successfully occupy a 0.2 spatial units inner diameter tube. When the filament is not long enough to wrap around the walls of the tubes, we observe a variety of helicoidal structures, governed by the elastic and twist parameters.

In our simulations, we tested two different set of constraints to maintain the thread inside the tubes. Total or partial suppression of the velocity in radial or axial direction is the fastest option to implement. However, it has appreciable effects in the results. Sudden reallocations and velocity dissipation artifacts multiply as more nodes are close to the tube walls. Alternatively, the penalty method applies a virtual force to all the nodes outside the restricted domain to promote an artificial displacement of the filament back into the inner part of the tube (in the radial direction). Determining the magnitude of the force that will push the nodes back to the tube, is critical for the stability of the simulation at long times. In our simulations the use of constant values for this force led to unstability. Using a dynamic force depending on the force vector acting on the nodes of the thread seemed to be a better option. Applying in the radial direction a fraction of the force mean value acting on all the nodes of the thread provided reasonable results even for long times.

he tube radius is increased, which is consistent when the thread length and the elastic parameters are fixed.

3.2. Axial displacement and fluid interaction

Helical structures are influenced by the presence of the fluid flow circulating through the tubes. Experimental video in Ref. [16] shows that helical structures in flow circuits move in the axial direction following the flow direction at a certain velocity. The velocities of the helical structures are very slow (in the order of 10^{-5} mm/s), which suggests low values for δ' in expression (13).

Under these circumstances we can implement this effect in the simulation by imposing the presence of a radius-dependant velocity profile (Hagen-Poiseuille equation) and use relation (8) to include the force exerted by the fluid on the thread. To avoid conflict between clamped boundary conditions at the thread ends and convective displacement, we move accordingly the filament ends. Each node is locally acted by fluid forces by means of equation (8), but simultaneously a net uniform displacement is induced because of action of the fluid in **X** direction. A value for such displacement may be given by the estimator σ:

$$\sigma = q\{1, 0, 0\} \cdot \bar{F}_x L \Delta\tau^2 \tag{15}$$

being q a fitting constant, $\bar{F}_x$ the mean value of the dimensionless fluid force acting on axial direction (**X** axis), L the length of the thread and $\Delta\tau$ the time step size. Supplementary Movie 2 shows the implementation of such mechanism in a growing thread to develop helices while the whole thread is flowing axially.

4. Biofilm streamer behavior in a corner flow

In Ref. [15] the formation of biofilm streamers inside piecewise rectangular channels is analyzed. Images and movies of these experiments reveal the formation of bacterial threads joining the corners of the circuit. A two-dimensional model of an elastic filament in a corner flow shows that under certain conditions filaments cross the main stream and reach the opposite corner [27]. As in the case of helices, this configuration seems to be a minimum of the elastic energy. Here we use a three dimensional discrete rod model to simulate the evolution of a biofilm filament (of fixed or increasing length) in a three dimensional corner geometry, see Figure 6. A liquid flowing through the channel exerts a force over the surface of the biomass, thus deforming and moving it. The velocity components and normalized modulus $\left|\vec{U}\right|$ in the central plane are illustrated in Figure 7. The three dimensional flow field was computed by using COMSOL multiphysics for the considered channel geometry, driven by a pressure drop. We keep this flow field during the whole simulation, ignoring perturbations due to the presence of the thin biofilm thread, as in [47, 27]. Simulations of thicker aggregates in similar flow geometries adapting the flow to shape changes of the aggregate were performed in [50].

4.1. Curved streamers

Our initial biofilm seed is an elastic filament of length L placed about the middle **XY** plane, with an initial inclination θ, and anchored at a small biomass spot that does not move. Only the thread is affected by the fluid flow. In this case study we integrated the evolution equation (13) by fixing the characteristic spatial length to be $\lambda = 1\ \mu m$ and the characteristic time of the system to be the elastic deformation time, leading to $\alpha' = 1$, $\beta' = \beta/\alpha$, $\delta' = \eta$ in equation (14). As mentioned, if we consider our thread to be isotropic, we have $\beta' = \frac{1}{2(1+\nu)}$.

We analyze the effect of parameter η (the fluid to elastic force ratio) in the final equilibrium position of the filament, and also analyze those features relevant for the dynamics of the elastic thread of the initial conditions: its initial length, its angle and its initial speed. Simulations showed that straight and curved filaments located out of the mid-plane tend to reallocate in a preferential **XY** plane close to it. Threads reach stationary positions in the channel or touch the opposite side depending on the combination of the studied variables.

The parameter η regulates the effect on the fluid on the thread dynamics. For values of $\eta \leq 4000$, the contact of the thread with the opposite corner is only dependant of the filament initial position and length. Concretely, we analyzed the success of different threads with different initial angle and length for a constant value $\eta = 3000$, fixing as initial velocity the velocity of the fluid in those positions. The results indicate that a minimum length is needed for the thread to reach the opposite corner. Figure 8(a) illustrates the influence of the initial length on successfully reaching the opposite corner. Notice that, although the distance between the anchoring point and the opposite corner is 121 spatial steps (chosen to be microns) a minimum length of 155 microns (a 28% more than the straight trajectory) is needed to cross the channel. A similar situation is encountered when the angle θ is changed, see figure 8(b). Angles above 20 degrees allow the thread to bend and touch the other side of the channel if the length of the thread is larger than 155 microns. Supplementary Movie 3 shows an animation of these examples.

Within the range $4000 < \eta < 8000$ the fluid can substantially modify the trajectory of the thread. For $\eta > 8000$ the fluid strongly drags the thread in the direction of the stream, avoiding any contact with the opposite corner. A steady position for the thread parallel to the streamlines but was found for η values around 30000, in accordance with the results obtained in the

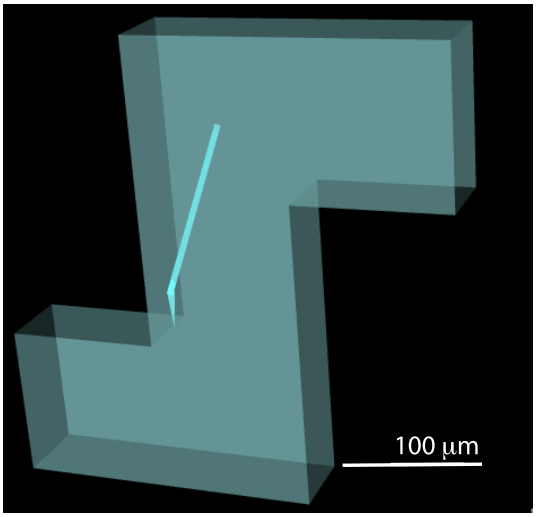

Figure 6: Three dimensional visualization of the initial filament configuration in the corner.

simulations of Reference [27].

The initial velocity of the thread is also important. Starting from a thread at zero velocity close to the wall, no simulations produced a contact with the other corner of the channel: very soft threads ($\eta \sim 30000$) were rapidly dragged by the flow and were aligned with the stream. Very low values of eta ($\eta \sim 30$) may approach the other side, but are not physically representative of the system we are modeling. As commented above, a thread velocity equal to the fluid velocity at the node positions allows to cross the mainstream depending on the initial position of the thread and its initial length. However, if we set an initial velocity in the $\mathbf{Y}$ direction the results change. The thread may now cross the channel when it is long enough enough provided the velocity modulus is high enough to exit zone I and enter zone II in Figure 7, where the fluid supports displacement in the $\mathbf{Y}$ direction.

The structure of the flow justifies these constraints. Figure 7(b) distinguishes three zones according to the leading velocity component. In zones I and III, the dominant components are vertical (positive $\mathbf{X}$ axis) and horizontal (positive $\mathbf{Y}$ axis) respectively. Zone II is the transition region, where both components are balanced and the flow follows a noticeably curved trajectory.

Short threads lying mostly in zone I are pushed parallel to the wall by the fluid. The thread swings, unable to reach the opposite corner. If part of the filament enters zone II, then the fluid will pull the thread into the channel

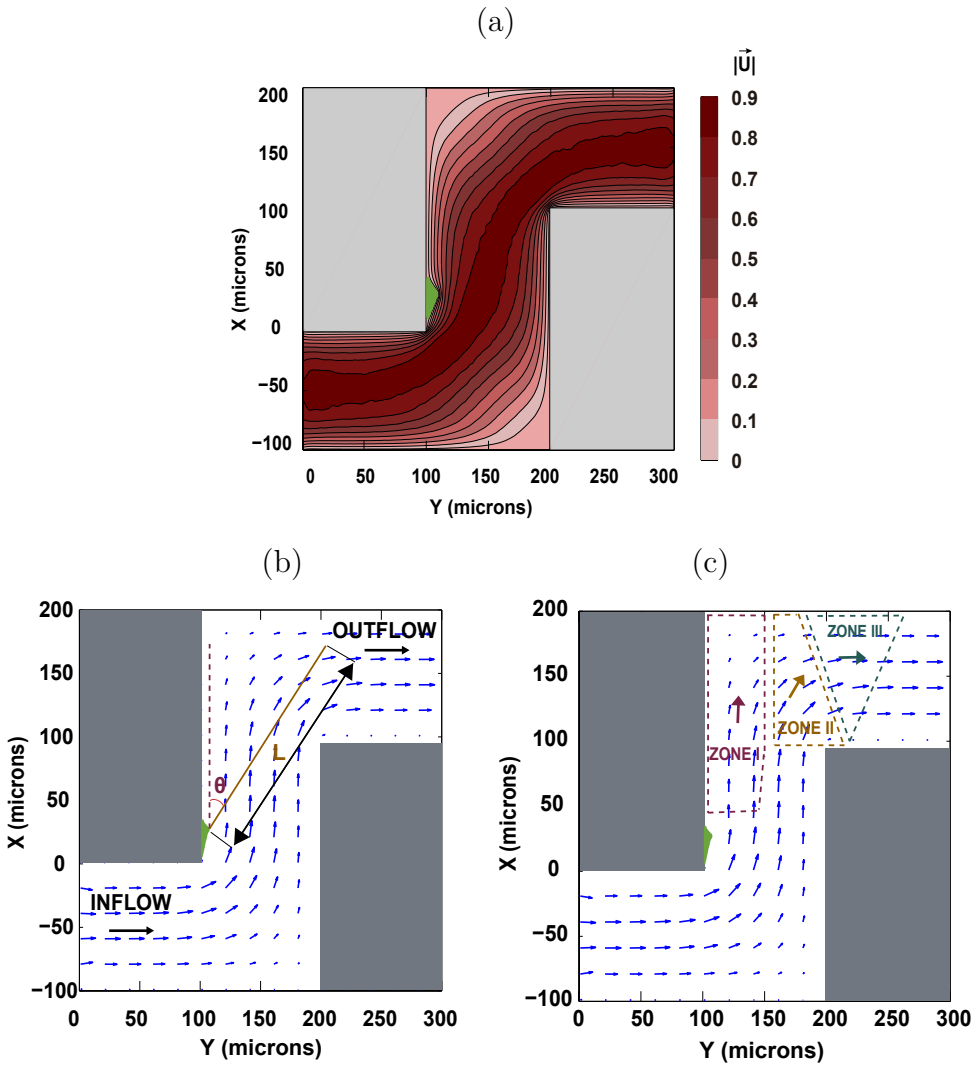

Figure 7: (a) Normalized velocity modulus contour in the mid-plane of the three dimensional channel. $\left|\vec{U}\right| = \frac{|\vec{u}|}{u_{max}}$, with $u_{max} = 1\,mm/s$. (b) Initial conditions for simulations of a thread with length L and angle θ. (c) Division of the corner section in three zones depending on the force component induced by the flow in the streamer.

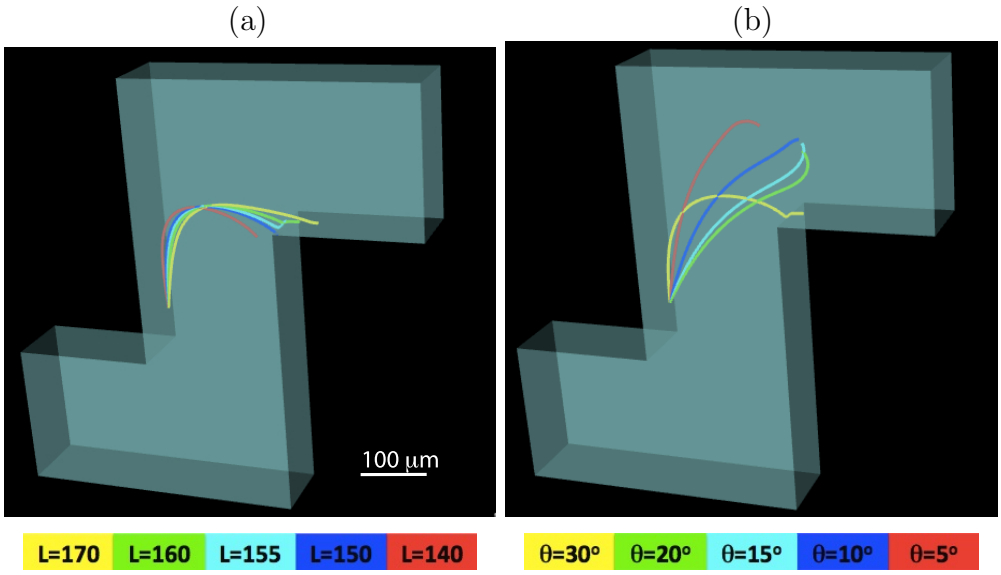

Figure 8: Effect of initial conditions in the simulation: (a) Length L and (b) angle θ. Length and orientation restrictions are required for the filament to cross the channel. Parameters for all cases are $\alpha' = 1$, $\beta' = 0.358$, $nodes = 100$, $\eta = 3000$, $\kappa = 0.05$, $\Delta\tau = 10^{-3}$ time units

following the fluid flow. A force competition is established within the thread. If the length is not large enough, we obtain a swinging movement unable to cross the channel. Larger lengths drive the filament into zone III, where fluid flow strongly drags the thread driving it to the other corner. The required lengths vary depending on the initial position of the streamer.

4.2. Growing curved streamers

The previous simulations consider a fixed filament length. However biofilms in those systems often suffer adhesion or stretching phenomena because of the interaction between the fluid and the nature of the biomass. We may implemented numerically such effects by increasing the length between nodes simultaneously at a fixed rate.

Succeeding on reaching the opposite corner is only possible provided that the filament could enlarge and reach zones II and III, thus allowing pulling forces to bend it. Ref. [51] contains an experimental video showing how a streamer joins both sides of the channel. Fluctuations in the upper left wall suggest a biomass flow close to the wall before the central streamer appears, which may indicate that the thread expands in length following

the wall and curve its trajectory helped by the change in direction present in the channel. Inspired by this mechanism, we have successfully simulated (see Supplementary Movie 4) the growth of streamers joining corners. An initially small thread is allowed to spread at a large fixed rate. The thread increases its length following the streamlines in that area, which naturally positions it parallel to the wall. The change of direction because of the presence of the upper corner generates a curved trajectory in the filament, allowing the thread to penetrate in the flow field. The fluid acts in this part of the thread by pulling it into the inner part of the channel. The combined action of the fluid and the sustained growth allow the thread to finally reach the opposite side.

Other mechanisms to reach the other corner could envisaged: a biomass thread sufficiently fast could reach the other side of the channel, but the speeds required for succeeding clearly overpass the fluid velocity, which makes no sense in the studied system.

5. Conclusions

In this work we reproduce the dynamics of three-dimensional biofilm threads immersed in a fluid flow, as experimentally observed in the laboratory. Coupling a discrete elastic rod model to an asymptotic law for the hydrodynamic forces on slender bodies we are able to reproduce helicoidal biofilm formation in circular tubes and biofilm streamer formation in corner flows. Numerical strategies are introduced to deal with the tube constraints and convective displacements. We conclude that filamentous biofilm behaviour can be described at laminar regimes by considering only its elastic deformation, its interaction with the surrounding fluid and the spatial restrictions that external constraints impose to the thread displacement. This agreement, together with the extreme simplicity of our model, suggest that the intrinsic biological complexity of these living aggregates diminishes in spatial and temporal scales in which fluid dynamics and solid mechanics govern their behaviour.

Acknowledgements. The authors thank H.A. Stone for insight on biofilms in flows, and J.H. Maddocks for insight on the mathematics of helical structures in nature. This research has been supported by MICINN-MINECO grants No. FIS2011-28838-C02 and No. MTM2014-56948-C2, CAM grant No. S2009/DPI-1559 and project C-ICT/3285 of the UE FP7.

References

[1] E. Ben-Jacob, I. Cohen & Herbert Levine, Adv. Phys. 49 (2000) 395-554.

[2] P. Watnick, R. Kolter. J. Bacteriol. 182 (2000) 2675-2679.

[3] L. Hall-Stoodley, J. W. Costerton, P. Stoodley, Nat. Rev. Microbiol. 2 (2004) 95-108.

[4] D. Dusenbery, Living at microscale, Harvard University Press 2011.

[5] S. Bardy, S. Ng, K. Jarrell, Microbiology 149 (2003) 295-304.

[6] J.W. Costerton, Z. Lewandowski, D.E. Caldwell, D.R. Korber, H.M. Lappin-Scott. Annu Rev Microbiol 49 (1995) 711-745.

[7] G.A. O'Toole , H.B. Kaplan, R. Kolter, Annu. Rev. Microbiol. 54 (2000) 49-79.

[8] J.W. Costerton, Philip S. Stewart, E. P. Greenberg. Science 284 (1999) 1318-1322.

[9] N. Hoiby, T. Bjarnsholt, M. Givskov, S. Molin, O. Ciofu, Int. J. Antimicrob. Agents 35 (2010) 322-32.

[10] H.C. Flemming, J. Wingender, Nat. Rev. Microbiol. 8 (2010) 623-633.

[11] M.J. McBride, Annu. Rev. Microbiol. 55 (2007) 49-75.

[12] T. Shaw, M. Winston, C.J. Rupp, I. Klapper and P. Stoodley, Phys. Rev. Lett. 93 (2004) 098102.

[13] B. Purevdorj, J.W. Costerton, P. Stoodley, Appl. Environ. Microbiol. 68 (2002) 4457-4464.

[14] J.B. Xavier, E. Martinez-Garcia, K.R. Foster, Amer. Naturalist 174 (2009) 1-12.

[15] R. Rusconi, S. Lecuyer, N. Autrusson, L. Guglielmini, H. A. Stone. Biophys. Journal 100 (2011) 1392-1399.

[16] D.R. Espeso, A. Carpio, E. Martinez-Garcia, V. de Lorenzo, Stenosis triggers spread of helical Pseudomonas biofilms in cylindrical flow systems, Scientific Reports 6 (2016) 27170.

[17] R.L. Scharf, J Food Prot. 75 (2012) 123-131.

[18] C.C. de Carvalho, Recent Pat. Biotechnol. 1 (2007) 49-57.

[19] P.W. Stone, Expert Rev. Pharmacoecon. Outcomes Res 9 (2009) 417-422.

[20] T. Shunmugaperumal, Biofilm eradication and Prevention. A pharmaceutical approach to medical device infections, John Wiley & Sons (2010).

[21] T. Storck, C. Picioreanu, B. Virdis, and D. J. Batstone, Biophys. J. 106 (2014) 2037-2048.

[22] D. Rodriguez, B. Einarsson, A. Carpio, Biofilm growth on rugose surfaces, Physical Review E 86 (2012) 061914.

[23] D. R. Espeso, A. Carpio, B. Einarsson, Differential growth of wrinkled biofilms, Physical Review E 91 (2015) 022710.

[24] N.G. Cogan, R.D. Guy, HFSP J. 4 (2010) 11-25.

[25] A. Seminara, T.E. Angelini , J.N. Wilking, H. Vlamakis, S. Ebrahim, R. Kolter, D.A. Weitz, M.P. Brenner, PNAS 109 (2012) 1116-1121.

[26] D. Taherzadeh, C. Picioreanu, U. Küttler, A. Simone, W.A. Wall, H. Horn, Biotech. Bioeng. 105 (2009) 600-610.

[27] N. Autrusson, L. Guglielmini, S. Lecuyer, R. Rusconi, H. A. Stone. Phys. fluids 23 (2011) 063602.

[28] E. Ben Jacob, I. Becker, Y. Shapira, H. Levine. Trends Microbiol. 12 (2004) 366-372.

[29] E.P. Fox, C.K. Bui, J.E. Nett, N. Hartooni, M.C. Mui, D.R. Andes, C.J. Nobile, A.D. Johnson, Mol. Microbiol. 96 (2015) 1226-1239.

[30] A.R. Hinkle, S. Goyal, H.J. Palanthandalam-Madapusi, J. Appl. Mech. - Trans. ASME 79 (2012) 051005.

[31] S. Goyal, N.C. Perkins, C.L. Lee, Int. J. Non-linear Mech. 43 (2008) 65-73.

[32] J.M.T. Thompson, M. Silveira, G.H.M. van der Heijden, M. Wiercigroch, Procs. Roy. Soc. A 468 (2012) 1591-1614.

[33] J. Valverde, G.H.M. van der Heijden, Int. J. Nonlinear Mechs. 47 (2012) 38-53.

[34] A. Majumdar, A. Goriely, Physica D - Nonlinear phenomena 253 (2013) 91-101.

[35] C.C. Lin, H.R. Schwetlick, J. Math. Chem. 45 (2009) 748-768.

[36] A.K. Tornberg, M.J. Shelley, J. Comp. Phys. 196 (2004) 8-40.

[37] A.l. Bobenko, Y.B. Suris, Comm. Math. Phys. 204 (1999) 147-188.

[38] R.S. Falk, J.M. Xu, SIAM J. Num. Anal. 32 (1995) 1185-1209.

[39] J. Chang, D.X. Shepherd, J.J. Zhang, Comput. Animat. Virtual Worlds 18 (2007) 429-436.

[40] J. Lenoir, S. Cotin, C. Duriez, P. Neumann, Computer & Graphics 30 (2006) 417-423.

[41] J. Brown, J.C. Latombe, K. Montgomery, Vis. Comp. 20 (2004) 165-179.

[42] Y. Yang, I. Tobias, W.K. Olson, J. Chem. Phys. 98 (1993) 1673-1686.

[43] I. Klapper, J. Comp. Phys. 125 (1996) 325-337.

[44] R.E. Goldstein, S.A. Langer, Phys. Rev. Lett. 75 (1995) 1094.

[45] J. Langer, D.A. Singer. SIAM Review 38 (1996) 605-618.

[46] M. Bergou, M. Wardetzky, S. Robinson, B. Audoly, E. Grinspun. ACM Trans. Graph. (SIGGRAPH) 27 (2008) 63.

[47] R.G. Cox. J. Fluid Mech. 44 (1970) 791-810.

[48] R. Goldenthal, D. Harmon, R. Fattal, M. Bercovier, E. Grinspun. ACM Trans. Graph. 26 (2007) 49.

[49] N. Chouaieb, A. Goriely, J.H. Maddocks, Procs. Nat. Acad. Sc. 103 (2006) 9398-9406.

[50] A. Carpio, B. Einarsson, D.R. Espeso, Dynamics of bacterial aggregates in microflows, ECMI 2014, eprints.ucm.es

[51] K. Drescher, Y. Shen, B. L. Bassler, H. A. Stone. PNAS 110 (2013) 4345-4350.